RESEARCH ARTICLE

Key Points:
- Multiple peaks in ring current ion flux are seen by stereo TWINS ENA images
- Enhanced spatial resolution obtained from TWINS stereoscopic ENA images
- THEMIS and GOES data support the ion flux obtained from TWINS ENA images

Correspondence to:
J. D. Perez,
perez@physics.auburn.edu

TWINS stereoscopic imaging of multiple peaks in the ring current

J. D. Perez[1], J. Goldstein[2,3], D. J. McComas[2,3], P. Valek[2,3], N. Buzulukova[4,5], M.-C. Fok[5], and H. J. Singer[6]

[1]Physics Department, Auburn University, Auburn, Alabama, USA, [2]Southwest Research Institute, San Antonio, Texas, USA, [3]Physics Department, University of Texas at San Antonio, San Antonio, Texas, USA, [4]NASA Goddard Space Flight Center/CRESST, Greenbelt, Maryland, USA, [5]NASA Goddard Space Flight Center, Greenbelt, Maryland, USA, [6]NOAA/National Weather Service, National Centers for Environmental Prediction, Space Weather Prediction Center, Boulder, Colorado, USA

Abstract Global, ion equatorial flux distributions and energy spectra are presented from stereoscopic Two Wide-Angle Imaging Neutral-Atom Spectrometers (TWINS) 1 and TWINS 2 energetic neutral atom (ENA) images for two time periods, 29 May 2010, 1330–1430 UT and 26 May 2011, 1645–1715 UT. The first is just after the main phase of a weak (minimum $SYM/H \approx -70$ to -80 nT) corotating interaction region-driven geomagnetic storm. The second is during a relatively quiet period. The global ion distributions show multiple spatial peaks that are coincident with peaks in the AE index. The energy spectra have a primary maximum in the 15–20 keV range. Below the energy maximum, the flux is Maxwellian. Above the main maximum, the flux is either significantly below that of a Maxwellian or has a second component with a maximum in the 40–50 keV range. For the 29 May 2010, 1330–1430 UT time period, the flux from the TWINS stereoscopic images is compared to the results from TWINS 1 and TWINS 2 alone illustrating the advantage of stereoscopic viewing. The flux deconvolved from the TWINS images also shows spatial and temporal correlations with Time History of Events and Macroscale Interactions during Substorms (THEMIS) in situ measurements. Magnetic field dipolarizations observed by GOES support the existence of a peak in the ion flux in the midnight/dawn sector. In summary, increased spatial resolution from TWINS stereoscopic ENA images is demonstrated. Multiple peaks in the ion flux of trapped particles in the ring current are observed. THEMIS electrostatic analyzer in situ ion flux measurements and GOES geosynchronous magnetic field measurements are consistent with the spatial and temporal structure obtained.

1. Introduction

There is considerable theoretical evidence for multiple injections of energetic ions into the ring current. *Erickson and Wolf* [1980] argued that because of pressure buildup, sunward convection from the plasma sheet must be time dependent. *Pontius and Wolf* [1990] first proposed the existence of bubbles in the magnetotail that would propagate earthward at high speed. *Chen and Wolf* [1993] connected the bubbles with observed bursty bulk flows [*Baumjohann et al.*, 1990]. *Chen and Wolf* [1999] developed a magnetohydrodynamic (MHD) theory for bubble propagation earthward from the plasma sheet in the form of bursty bulk flows. *Zaharia et al.* [2006] showed plasma pressure plots obtained from self-consistent modeling of magnetic fields that indicated possible multiple pressure peaks in the inner magnetosphere. *Goodrich et al.* [2007] modeled sawtooth events using the Lyon-Fedder-Mobarry global MHD simulations to obtain intermittent and patchy reconnection that result in associated flows in the inner magnetosphere which could lead to the multiple peaks in the ring current presented in this study. *Birn et al.* [2011] used 3-D MHD simulations of magnetic reconnection in the magnetotail to model bursty bulk flow and cross-tail structure producing earthward propagating dipolarization events which also may result in the multiple peaks described in this study. *Yang et al.* [2011] performed a simulation of fast earthward propagation of an idealized plasma sheet bubble injection using the Rice Convection Model with an equilibrated magnetic field model (RCM-E) [*Toffoletto et al.*, 2003] leading to substorm particle injections that may produce multiple peaks in the ring current. *Lin et al.* [2014] investigated storm time ion injection using a 3-D global hybrid simulation with a steady southward interplanetary magnetic field (IMF). Sample results are shown in Figure 1. Multiple flux ropes, *a–f*, are shown in the magnetotail. Flux rope *a* is near midnight, *b–d* are on the duskside, and *e* and *f* are on the dawnside. Flux rope *d* and *e* are moving earthward while *a–c* and *f* are moving tailward. Once an earthward flux rope reaches the inner magnetosphere, they are not resolved in this model.
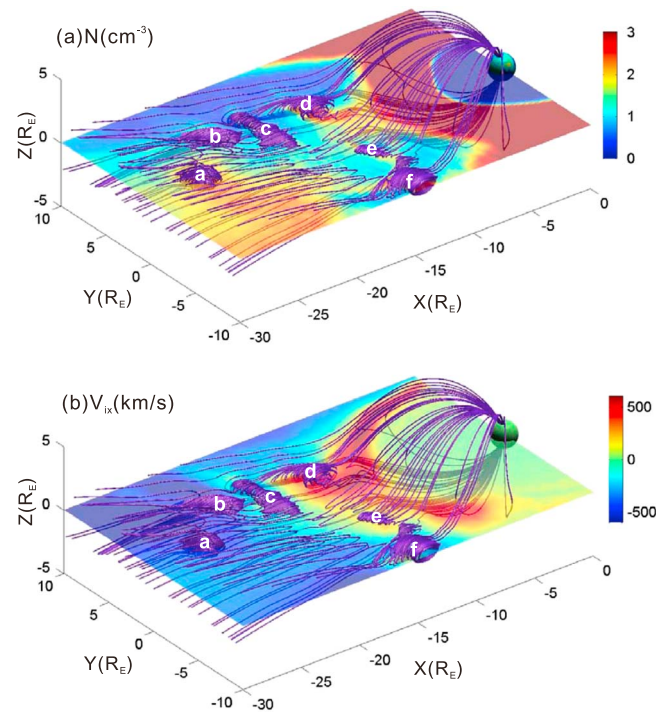
Figure 1. Results from 3-D hybrid global simulation [*Lin et al.*, 2014] showing multiple flux ropes with more on the duskside. (a) The ion density in the GSM equator of the magnetotail along with illustrative magnetic field lines. Flux ropes are marked with letters a–f. (b) The corresponding *x* component of the average ion velocity. (For an explanation of how the flux ropes are identified, see *Lin et al.* [2014].)

The predominance of injections on the duskside is attributed to the lower density in the tail resulting in a thinner cross-tail current sheet. It is to be noted that the above referenced calculations do not explicitly mention multiple peaks in the trapped particle ring current. Rather, they provide context and geophysical significance for the results of this study.

Experimental support for time dependent, patchy injections from the plasma sheet into the Earth's inner magnetosphere is also extensive. *Baumjohann et al.* [1990] first observed high-speed flows in the inner plasma sheet. *Angelopoulos et al.* [1992] first referred to them as bursty bulk flows and showed features of their temporal and spatial structure. *Sergeev et al.* [1996] observed high-speed flows consistent with the theoretical predictions of *Pontius and Wolf* [1990] and *Chen and Wolf* [1993]. The observation of sawtooth events [*Belian et al.*, 1995], i.e., quasi-periodic injections into the inner magnetosphere, also suggests the possibility of multiple peaks in the trapped ring current ions.

Huang et al. [2003] used multiple space-based and ground-based observations to demonstrate features that represent particle injections from the tail into the inner magnetosphere. *Henderson et al.* [2006a, 2006b] showed that sawtooth events on 10 and 11 August 2000 and 18 April 2002 were clearly associated with substorms. *Gabrielse et al.* [2014] studied more than 1000 ion injections as observed in the THEMIS (Time History of Events and Macroscale Interactions during Substorms) mission [*Angelopoulos*, 2008]. They found that injections into the inner magnetosphere are correlated with reconnection phenomena such as fast flows, and that such injections happen more often in the dusk/midnight sector than in the midnight/dawn sector. This corroborated a pattern observed by geosynchronous satellites [*Thomsen et al.*, 2001].

There have been a number of studies that have shown global images of ion flux obtained from the Imager for Magnetopause-to-Aurora Global Exploration (IMAGE) ([*Burch*, 2000]/medium energy neutral atom (MENA) [*Pollock et al.*, 2000] and high-energy neutral atom (HENA) [*Mitchell et al.*, 2000]) instruments and TWINS [*McComas et al.*, 2009a] single spacecraft ENA (energetic neutral atom) images. Using a method very similar to the one used in this study, ion flux global images from both IMAGE MENA and HENA ENA images gave indications of multiple spatial peaks in the inner magnetospheric ring current [*Perez et al.*, 2001; *Perez et al.*, 2004a, 2004b; *Zhang et al.*, 2005]. Similarly, using a different approach to extracting ion distributions from the IMAGE/HENA ENA images [*C:son Brandt et al.*, 2002a; *DeMajistre et al.*, 2004] showed indications of more than a single spatial peak in the trapped ion ring current [*C:son Brandt et al.*, 2002a, 2002b, 2002c; *C:son Brandt et al.*, 2004; *DeMajistre et al.*, 2004; *Vallat et al.*, 2004]. *Perez et al.* [2012] used TWINS 2 ENA images to examine three time periods during a CIR (corotating interaction region) driven storm on 22 July 2009, i.e., 0300–0600 UT (main phase), 0800–1000 UT (second *SYM/H* minimum), and 1100–1130 UT (recovery period). All but the recovery period showed evidence of multiple spatial peaks in the trapped ion flux. In this study, we use stereoscopic ENA images from TWINS 1 and TWINS 2 to produce improved resolution and show global images from two different time intervals that clearly show multiple peaks in the trapped ion distribution. Energy spectra at the location of the spatial peaks in the equatorial ion

flux are also presented showing indications of energy-dependent drift and the existence of two energy populations possibly associated with multiple injections.

In section 2, the sources of the data and the analysis methods used in this study are described. Examples of deconvolved ion flux from TWINS 1 alone, TWINS 2 alone, and combining TWINS 1 and 2 for stereoscopic views are compared with THEMIS in situ ion flux measurements for the 1330–1430 UT, 29 May 2010 time period. The increased spatial resolution due to stereoscopic viewing is demonstrated. In section 3, the global images of the ion flux in the trapped particle region of the ring current obtained from the stereoscopic TWINS ENA images are shown for the two time periods. The interval 1330–1430 on 29 May 2010 is just after the minimum *SYM/H* is reached in a CIR-driven storm. The interval 1645–1715 UT on 26 May 2011 is during a relatively quiet time. Multiple peaks in the spatial distributions are found in both. The energy spectra obtained at the peaks of the equatorial distributions are also shown. The non-Maxwellian features may be a result of energy-dependent drift and a second plasma component. The results are discussed in section 4 where GOES magnetic field data at geosynchronous orbit are shown to be consistent with an ion flux peak on the dawnside during the 1330–1430 UT on 29 May 2010 event. The study is summarized in section 5.

2. Data Sources and Analysis Techniques

2.1. Solar Wind and Geomagnetic Indices

In order to put the time periods treated in this study in context, solar wind parameters and geomagnetic activity indices are used from the OMNI website, http://omniweb.gsfc.nasa.gov/omsc_min.html. NASA's Space Physics Data Facility gathers data from satellite missions ACE, Wind, IMP8, and Geotail along with the bow shock model of *Farris and Russell* [1994] and the magnetopause model of *Shue et al.* [1997] to produce the parameters as a function of time shifted to the bow shock nose.

2.2. GOES Measurements of Magnetic Field in Geosynchronous Orbit

The National Oceanic and Atmospheric Administration (NOAA) Geostationary Operational Environmental Satellites (GOES) provide vector magnetic field measurements and very high-energy electron, proton, and alpha (hundreds of keV to multi-MeV) fluxes. Beginning with the new series of GOES satellites (GOES 13, 14, and 15) in addition to the high-energy particles, ions are now measured as low as 80 keV and electrons down to 30 keV but the measurements do not extend to the lower energy range treated in this study. Data from four of the GOES satellites, i.e., GOES 11, 12, 13, and 14 are available for the time periods of interest in this study.

2.3. THEMIS

Data from the electrostatic analyzer (ESA) [*McFadden et al.*, 2008] on board the THEMIS (Time History of Events and Macroscale Interactions during Substorms) E satellite is used to provide in situ measurements to be compared with the ion flux obtained from the stereoscopic TWINS ENA images. While the THEMIS ESA instrument measures energetic particles from a few eV up to 25 keV, we use the 15 keV results in this study. The THEMIS results used in this study have background subtracted and are mapped to the solar magnetospheric (SM) [*Russell*, 1971] SM equator using the same magnetic field model used in deconvolving the ion flux from the TWINS stereoscopic ENA images. Confidence levels for the THEMIS measured flux are estimated to be 10% (V. Angelopoulos, private communication, 2012).

2.4. TWINS
2.4.1. TWINS Data
A full description of the NASA TWINS (Two Wide-Angle Imaging Neutral-Atom Spectrometers) mission of opportunity is given in *McComas et al.* [2009a] and *Goldstein and McComas* [2013]. The two spacecraft are in Molniya orbits with inclinations of 63.4°, perigee altitudes of ~1000 km, and apogees in the Northern Hemisphere at ~7.2 R_E. The spacecraft are three-axis stabilized and provide approximately nadir pointing of the TWINS instruments. Because the orbital planes of the two spacecraft are significantly offset, the pair provides a combination of continuous magnetospheric observations from at least one TWINS satellite with several hours of simultaneous, dual platform viewing each orbit. In this study, we focus upon these latter times when TWINS 1 and TWINS 2 provide simultaneous, stereoscopic ENA images.
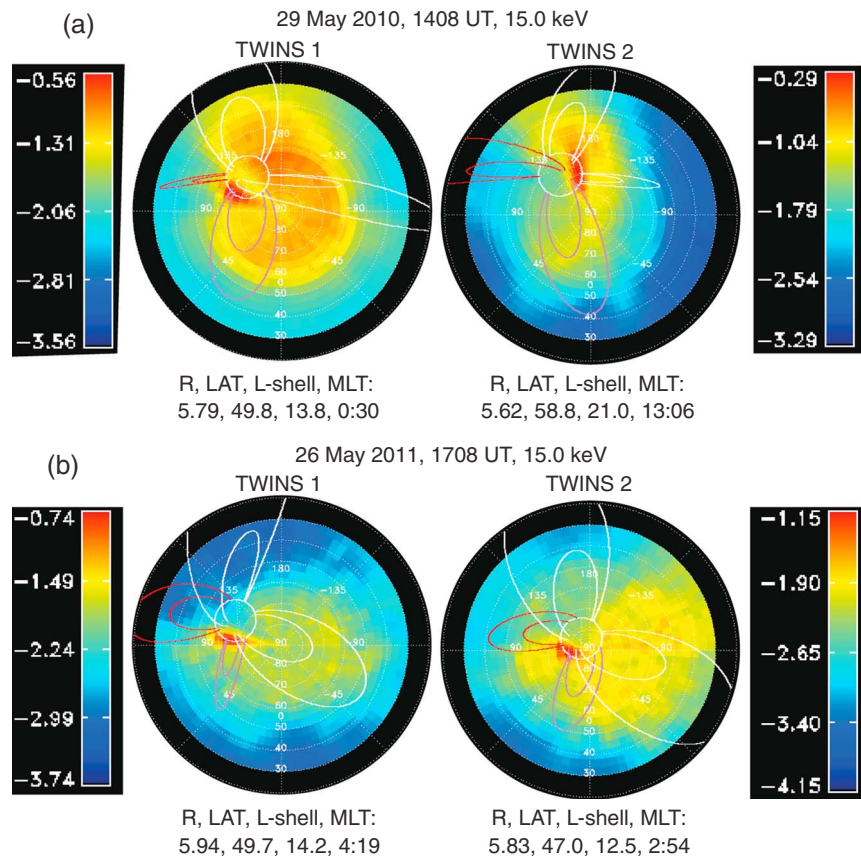
(a) 29 May 2010, 1408 UT, 15.0 keV

TWINS 1 — R, LAT, L-shell, MLT: 5.79, 49.8, 13.8, 0:30

TWINS 2 — R, LAT, L-shell, MLT: 5.62, 58.8, 21.0, 13:06

(b) 26 May 2011, 1708 UT, 15.0 keV

TWINS 1 — R, LAT, L-shell, MLT: 5.94, 49.7, 14.2, 4:19

TWINS 2 — R, LAT, L-shell, MLT: 5.83, 47.0, 12.5, 2:54

Figure 2. ENA images from TWINS 1 and TWINS 2 on (a) 29 May 2010, 1408 UT and (b) 26 May 2011, 1708 UT, all in the energy interval centered at 15.0 keV that extends from 7.5 to 22.5 keV. The units are the log of #/(s eV sr cm^2).

The TWINS instruments normally acquire full images every 78 s with an integration time of 60 s. The ENA images used in this study are integrated over 15–16 sweeps corresponding to ~15 min of observation time during a ~20 m time period. For this study, the two satellites are at approximately 6 R_E and move approximately $\frac{1}{3} R_E$, 2° latitude and 13 min magnetic local time (MLT) during the time periods analyzed in this study. Therefore, the small movement of the satellite during the image integration times compared to the size of the pixels is not expected to significantly affect the results of this study. The analysis of the images is done treating the location of the satellites as the midpoint during the appropriate time interval. A full description of the instruments is given by *McComas et al.* [1998].

The TWINS imagers are based upon the "slit camera" concept [*McComas et al.*, 1998] originally flown on the IMAGE satellite in the MENA instrument. This design provides the very large aperture, and hence geometric factor, required to properly image ENAs across the critical energy range from ~1 keV to 100 keV. For TWINS, a full image is acquired using two sensor heads that are mounted together on a rotating actuator, which sweeps back and forth over an approximately Earth-centered viewing cone. Neutral atoms are detected with energies from 1 to 100 keV with $\Delta E/E = 1.0$ for H atoms. Full images, i.e., a full angular sweep of both heads, are taken generally every 78 s with each having a 60 s integration time.

The TWINS images used in this study are processed using a statistical smoothing technique along with a background suppression technique described in detail in Appendix A of *McComas et al.* [2012]. This approach has also been applied successfully to ENA measurements on Interstellar Boundary Explorer [*McComas et al.*, 2009b].

Representative neutral images from both TWINS 1 and TWINS 2 for the two time periods in this study are shown in Figure 2. The brightest pixels in each of the images are along the limb of the Earth and are believed to be due to charge exchange of ions with neutral oxygen at low altitude (< 1000 km). These are the so-called LAEs (low altitude emissions) [*Roelof*, 1997]. The neutral emissions at higher altitude
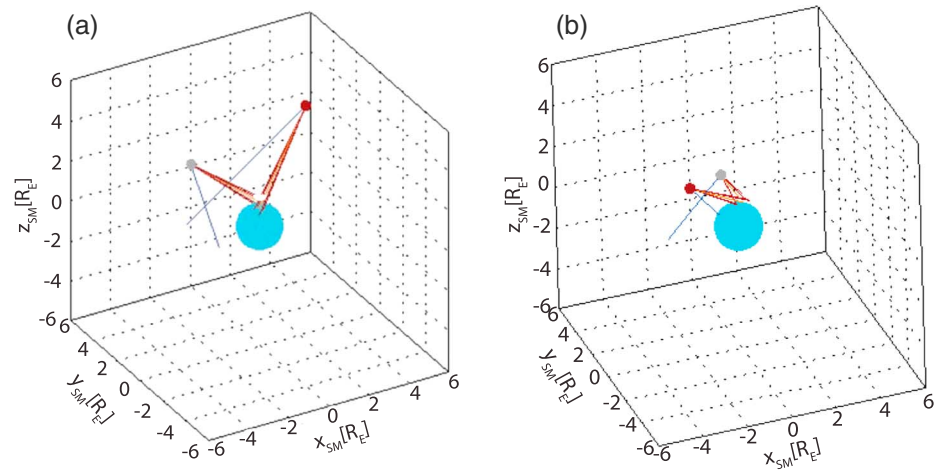
Figure 3. Three-dimensional illustration of the stereoscopic TWINS viewing configurations. The blue sphere is the Earth, the silver sphere TWINS 1, and the maroon sphere TWINS 2. The blue lines are the central lines of sight. The maroon solid angle emanating from each satellite is the field of view of the pixel with the maximum ENA flux in the images. The Sun is to the right in each plot. (a) 29 May 2010, 1408 UT. (b) 26 May 2011, 1653 UT.

(high altitude emissions) originate from charge exchange of the ions with neutral hydrogen in the Earth's geocorona and are less intense. (Note that the plots are neutral atom flux on a log scale.) For the 29 May 2010, 1330–1430 UT event, the TWINS 1 and TWINS 2 imagers are both at high altitude but TWINS 1 is on the nightside at 0030 MLT and TWINS 2 is on the dayside at 1306 MLT. For the 26 May 2011, 1630–1730 UT event, both TWINS 1 and TWINS 2 are in the midnight/dawn sector at 0419 MLT and 0254 MLT, respectively. The stereoscopic viewing geometry is shown in Figure 3. The lines of sight of the brightest pixels either hit the Earth or just graze it.

2.4.2. Ion Flux From Simultaneous TWINS 1 and TWINS 2 ENA Images

A technique for extracting equatorial ion pitch angle distributions from ENA images is described in Appendix A of *Perez et al.* [2012]. In this method, the ion equatorial pitch angle distribution is expanded in a linear combination of tricubic splines [*deBoor*, 1978]. The expansion coefficients are then obtained by minimizing a combination of normalized chi-squared and a penalty function derived by *Wahba* [1990]. Requiring that normalized chi-squared is near unity ensures that the resulting distribution fits the data. Including the penalty function in the minimization ensures that the result is as smooth (in the sense of a minimum second derivative) as is consistent with fitting the data. In this procedure, spatial structure is minimized and appears in the result only to the extent that it is necessary. Thus, while there may be more and smaller-scale structure that is not resolved, the structure that is found is statistically required to fit the data, i.e., match the ENA images.

The uncertainties in each pixel are a statistical measure of the information content in the ENA images. In this study, the second moment of the 15–16 individual sweeps is used to estimate the uncertainties in each pixel of the time-integrated image.

In order to obtain sufficient counts to construct a meaningful image, the TWINS ENA images used in this study are integrated over energy bands whose width is equal to the central energy, e.g., the 15.0 keV images are integrated from 7.5 to 22.5 keV. To account for the overlap of the measured energy bands, particularly at higher energy, after the equatorial ion intensities integrated over pitch angle are determined at the central energies as described in Appendix A of *Perez et al.* [2012], the physically meaningful energy spectra are obtained using a method described in Appendix B of *Perez et al.* [2012].

In order to deconvolve the ion distributions, magnetic field mapping is required. For this study the *Tsyganenko and Sitnov* [2005] magnetic field model was used. The density of neutral hydrogen, i.e., the geocorona, is also needed. The TWINS exospheric neutral hydrogen density model was used [*Zoennchen et al.*, 2013]. To include the LAEs, the thick target approximation of *Bazell et al.* [2010] was used.

To illustrate the advantages gained by using simultaneous TWINS 1 and TWINS 2 ENA images, i.e., stereoscopic viewing, we compare the resulting ion flux from TWINS 1 and TWINS 2 alone and in
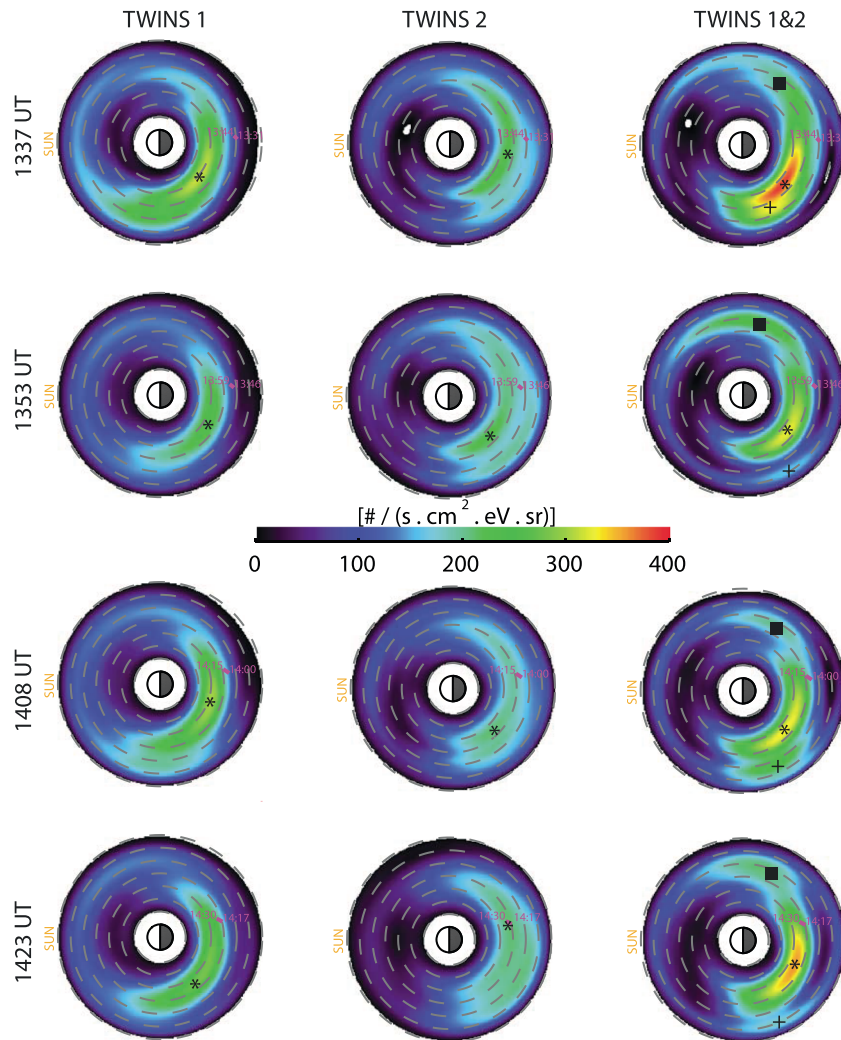
Figure 4. Comparison of equatorial pitch angle averaged ion flux at 15.0 keV obtained from TWINS 1 and 2 alone and combined for 15 sweep periods centered at 1337, 1353, 1408, and 1423 UT on 29 May 2010. The Sun is to the left in all plots. The radius extends to 8 R_E. Distances are marked in 1 R_E intervals by gray dashed circles. The principal peak of the ion flux is marked by a black star. Additional peaks are marked by a black plus sign and black square in the ion flux from the stereoscopic TWINS results. The same color bar is used for all plots.

combination in Figure 4 for four time intervals centered at 1337, 1353, 1408, and 1423 UT on 29 May 2010. We see that the derived spatial distributions are, of course, not exactly the same. The primary differences are (1) the higher and sharper main spatial peak in the ion flux at 4.5 R_E in the dusk/midnight sector marked by a black star in all the frames, (2) a more clearly defined spatial peak in the ion flux at 7.0 R_E in the dusk/midnight sector marked by a black plus sign in the right-hand column, and (3) a distinct peak in the midnight/dawn sector that is only visible in the ion flux deconvolved from the combined TWINS 1 and 2 results shown in the third column marked by a black square. More information about the results from the stereoscopic views, cf. Figure 7, will be given in the following sections. Here the emphasis is on the enhanced spatial resolution provided by stereoscopic viewing.

In Figure 5, the TWINS results are compared with THEMIS E in situ measurements. The red curve from the stereoscopic view of both TWINS 1 and TWINS 2 gives a somewhat better match to the in situ measurements. While the slopes of the TWINS 1 and combined TWINS 1 and TWINS 2 results are similar, the green curve of TWINS 1 alone has a consistently lower ion flux than the TWINS 1 and TWINS 2 result, whereas the blue curve from TWINS 2 alone is essentially flat during the four-time interval, i.e., it does not follow the spatial variations of the in situ measurements as well as the stereoscopic result. It is to be noted that TWINS 2 alone results were
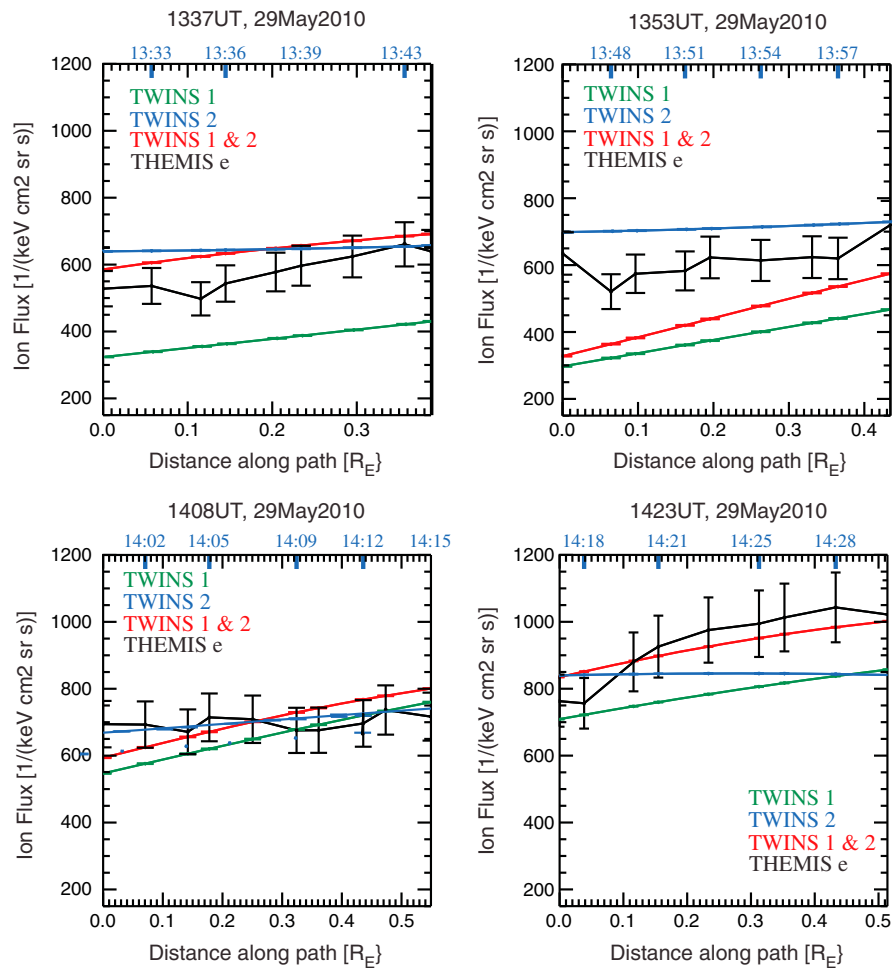
Figure 5. Comparison of ion flux at 15.0 keV obtained from TWINS 1, TWINS 2, and TWINS 1 and 2 combined with THEMIS E in situ measurements for 1337, 1353, 1408, and 1423 UT on 29 May 2010. The TWINS ion flux values are multiplied by a factor of 4 to highlight the relative spatial and temporal agreement. The lower horizontal axis is the distance along the THEMIS path shown in Figure 2 by the purple line. The upper horizontal axis is UT along the path. The THEMIS error bars are estimated to be 10%. The small error bars on the deconvolved results from TWINS are discussed in *Perez et al.* [2012].

compared with the in situ THEMIS results in a previous study emphasizing the pitch angle distributions [*Grimes et al.*, 2013]. Since THEMIS only observes along a single path through the global image obtained from the TWINS observations, this comparison does not unequivocally distinguish either one of the three results from one another. The information that is obtained from single TWINS 1 or TWINS 2 images does provide valuable context for in situ measurement. It is the enhanced spatial structure in the global image obtained from the combined TWINS 1 and TWINS 2 images that illustrate the advantage of stereoscopic viewing.

The THEMIS points in Figure 5 are not indicative of either the time or spatial resolution of either the THEMIS or the TWINS results. The THEMIS ESA instrument has a 3 s spin period giving it much higher temporal resolution than shown here. Also, temporal and spatial resolutions are mixed in the THEMIS measurements. As stated above, the TWINS images are integrated over approximately 15 min time intervals. Even though the size of the TWINS pixels used in this analysis, 4° × 4°, is known, it is not possible to quantify the spatial resolution of the TWINS observations because the deconvolution process by which the ion distributions are obtained from the ENA images selects the spatially smoothest distribution that is consistent with the data. This fact, of course, enhances the validity of the multiple peak structures presented in this study. It is, therefore, expected that THEMIS observations will generally have greater variations in both time and space.

In Figures 4 and 5, the TWINS ion flux is multiplied by a factor of 4 in order to more clearly visualize the agreement between the spatial and temporal variations in the global images and the in situ measurements.
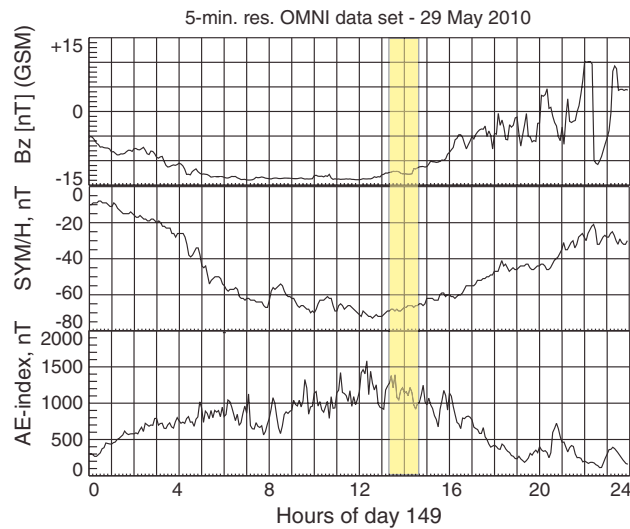
Figure 6. The *z* component of the interplanetary magnetic field in the GSM coordinate system scaled in time to the nose of the magnetopause and geomagnetic activity indices, *SYM/H* and *AE*, from the OMNI data website (http://omniweb.gsfc.nasa.gov/form/omni_min.html) for 29 May 2010. The time period with stereoscopic TWINS ENA images treated in this study is marked by the yellow rectangle.
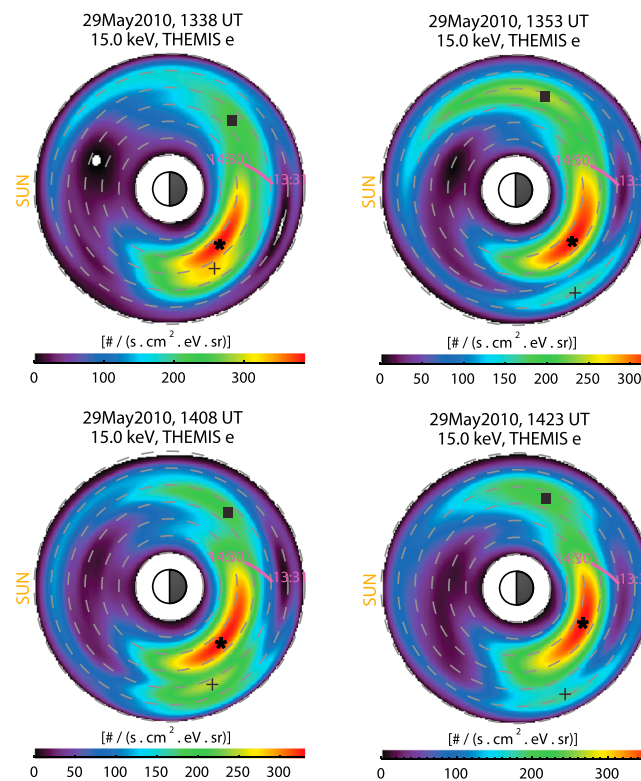

Figure 7. Equatorial pitch angle averaged ion flux at 15.0 keV on 29 May 2010 for times 1338, 1353, 1408, and 1423 UT. The THEMIS E path from 1331 to 1430 UT is shown as a purple line. The location of the peak of the ion flux is indicated by black stars. A second peak is indicated by black plus signs. A third peak is noted by black squares. Color bars are slightly different to emphasize the spatial distributions.

The factor 4 is for this event only, but it is not unusual for the magnitude of the ion flux obtained from ENA images and in situ measurements to differ. This was first noted in a comparison of IMAGE/HENA images and Cluster measurements [*Vallat et al*., 2004]. It has also been observed in previous comparisons of TWINS and THEMIS results [*Grimes et al*., 2013] using the same methodology used here, and more recently by *Keesee et al*. [2014] using a completely different analysis approach. Numerical simulations of ring current dynamics using the CIMI (Comprehensive Inner Magnetosphere Ionosphere) model also give higher ENA flux than observed by TWINS [*Fok et al*., 2014]. As discussed in *Perez et al*. [2012] the statistical confidence levels in the deconvolved ion flux are very small, but this does not represent the real uncertainty in the result. The use of (1) a model magnetic field to map to the SM equator, (2) the assumption of conservation of the first adiabatic invariant, (3) a model of the density of the geocorona, and (4) the assumption that all the ions are hydrogen, all contribute to uncertainties that cannot be quantified. This contributes to uncertainty in the spatial dependence and in the overall magnitude of the deconvolved ion flux. It is, however, expected that, while the uncertainties introduced by these assumptions are not random, they will not necessarily bias the results in one way or another.

3. Results

In this section, we present results from the analysis of stereoscopic ENA images for two events that have different solar wind and geomagnetic activity parameters. Both show multiple spatial peaks in the ion flux that occur at times of relatively high *AE* index. Both also show energy spectra that have high-energy tails that fall below comparable Maxwellian distributions and/or high-energy maxima suggesting a second plasma population in the energy spectra.
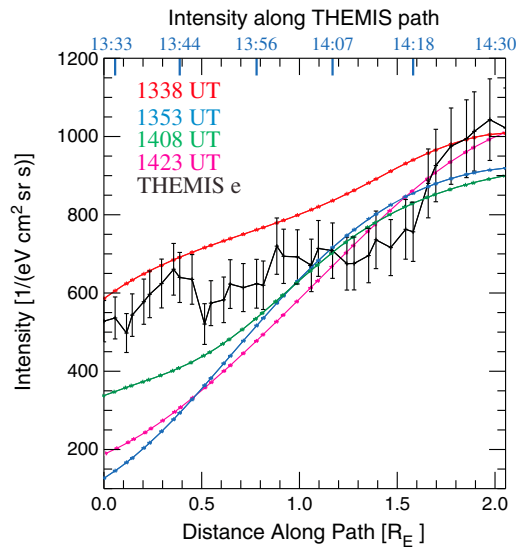
Figure 8. Comparison of TWINS 1 and 2 ion flux as a function of position and time compared with THEMIS E in situ measurements for 1338, 1353, 1408, and 1423 UT on 29 May 2010. The energy is 15.0 keV. The lower horizontal axis is distance along the path shown in Figure 6. The upper horizontal axis is time in UT. The TWINS ion flux is an average over approximately 15 min centered on the times shown, while the THEMIS results vary directly with time. As discussed in section 2.4.2, the TWINS results are multiplied by a factor of 4.

3.1. Event 1: 29 May 2010, 1330–1430 UT

Figure 6 shows the OMNI data for the entire day 29 May 2010. Note that the z component of the interplanetary magnetic field shown in the top panel is steady for approximately 10 h before the time period, 1330–1430 UT that is focused upon in this study. This is a relatively weak CIR storm [*Grimes et al.*, 2013] with a minimum SYM/H of about −70 nT just prior to the time period of interest here. Of special note is the fact that AE is above 1000 nT for several hours with peaks near 1500 nT between 1200 and 1300 UT just before the period of focus in this study and near 1300 nT between 1300 and 1400 UT during the period of focus in this study.

Figure 7 shows the deconvolved equatorial pitch angle averaged ion flux obtained from stereoscopic TWINS 1 and TWINS 2 ENA images for four sequential 15 min time periods plotted on the same color bars to illustrate the time dependence of the magnitude of the ion flux. They are a repeat of the results in the right-hand column of Figure 4 where they were plotted with different color bars to highlight the temporal dependence of the spatial variations.
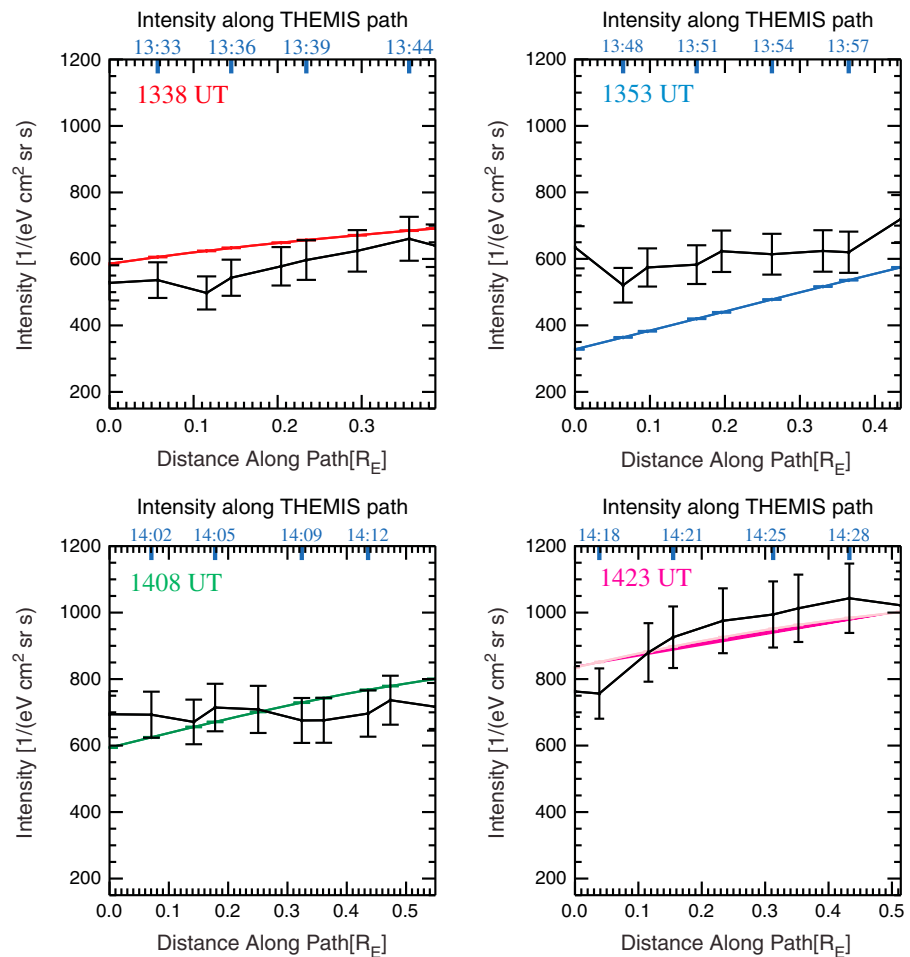
The brightest peak, shown with black stars, is between 4 and 5 R_E in the late dusk/midnight sector. A second peak marked by black plus signs, is visible in the images at 1353, 1408, and 1423 UT at 5.5–7.0 R_E in the early dusk/midnight sector. A third peak, noted with black squares, is between 5 and 6 R_E in the midnight/dawn sector.

In Figures 8 and 9, we show, in a different format, the good agreement between the spatial dependence of the results from the TWINS stereoscopic views and the THEMIS in situ measurements. In Figure 8, the TWINS results for the four different times are plotted over the full range of the THEMIS path during the period 1333–1430 UT. It is important to note that the TWINS results are a function of position for a specific 15 min time period, while the THEMIS results are a simultaneous function of space and time. We see that the TWINS result for 1338 UT is consistent with the THEMIS result for the first 0.5 R_E of the THEMIS path, whereas the TWINS results for the other 3 times are below the THEMIS result. This could well be due to time dependence, i.e., during the subsequent three time periods, the ion flux at the beginning of the THEMIS path may have decreased. To illustrate this more clearly, in Figure 9, the TWINS results during the four sequential 15 min time periods are compared to the THEMIS measurements only during the same time period. Only during 1345–1400 UT are the TWINS results noticeably different than the in situ THEMIS measurements.

It is not at all surprising that THEMIS spatial dependence shows more structure than TWINS. The spatial resolution of the ENA images cannot compete with the in situ measurements. What the TWINS stereoscopic images do provide is a complete equatorial view, albeit at lower resolution, of trapped ions in the ring current. This capability indicates that multiple peaks in the ring current exist simultaneously—something that cannot be determined with even a reasonable number of in situ spacecraft.

Figure 10 shows ion flux energy spectra obtained from the TWINS ENA images (green solid line) compared to a Maxwellian with the same peak energy (purple dashed line) for the four time periods centered at 1338, 1353, 1408, and 1423 UT on 29 May 2010. The three columns are for the three peaks shown in Figure 7. For the main peak (cf. Figure 7, black star), the one with a radius of approximately 4.5 R_E in the premidnight sector, the distributions are Maxwellian below the maximum energy between 15 and 20 keV, but above the maximum it is below the Maxwellian with an equivalent maximum energy. For the secondary peak, at larger

Figure 9. Ion flux obtained from stereoscopic TWINS 1 and 2 images are compared with THEMIS E in situ measurements as a function of position and time for the specific time intervals in which the TWINS 1 and 2 results were obtained, i.e., those centered at 1338, 1353, 1408, and 1423 UT. As discussed in section 2.4.2, the TWINS results are multiplied by a factor of 4.

radius, i.e., between 5.5 and 7.0 R_E in the dusk/midnight sector (cf. Figure 7, plus sign), there is a maximum in the energy spectra between 10 and 15 keV and another higher-energy maximum at about 40 keV which by 1423 UT is stronger than the lower energy maximum. For the third peak at about 5.5 R_E in the midnight/dawn sector (cf. Figure 7, black square), the distribution is initially Maxwellian with a maximum at about 15 keV. In the next half hour a second energy maximum at about 45 keV appears but disappears by 1423 UT.

For these energies at these distances from the Earth, the sum of the magnetic curvature and drift velocities are of the order 5–10 R_E/h for a dipole magnetic field. Therefore, it is possible that the observed multiple peaks are due to drifts rather than different injections. But the observed images are not able to make that distinction. Numerical simulations of the motion and lifetime of ions in the inner magnetosphere perhaps coupled to simulations of injections from the magnetotail are necessary to fully understand this phenomenon.

3.2. Event 2: 26 May 2011, 1645–1715 UT

Figure 11 shows the OMNI data for the entire day 26 May 2011. We are able to deconvolve ion flux from stereoscopic TWINS 1 and TWINS 2 ENA images for the time period 1645–1715 UT. B_z is oscillating between −2 and −6 nT, and *SYM/H* is just barely negative. But there is some indication of geomagnetic activity as *AE* makes a sharp rise just past 1600 UT, but only reaches a peak value of about 400 nT.
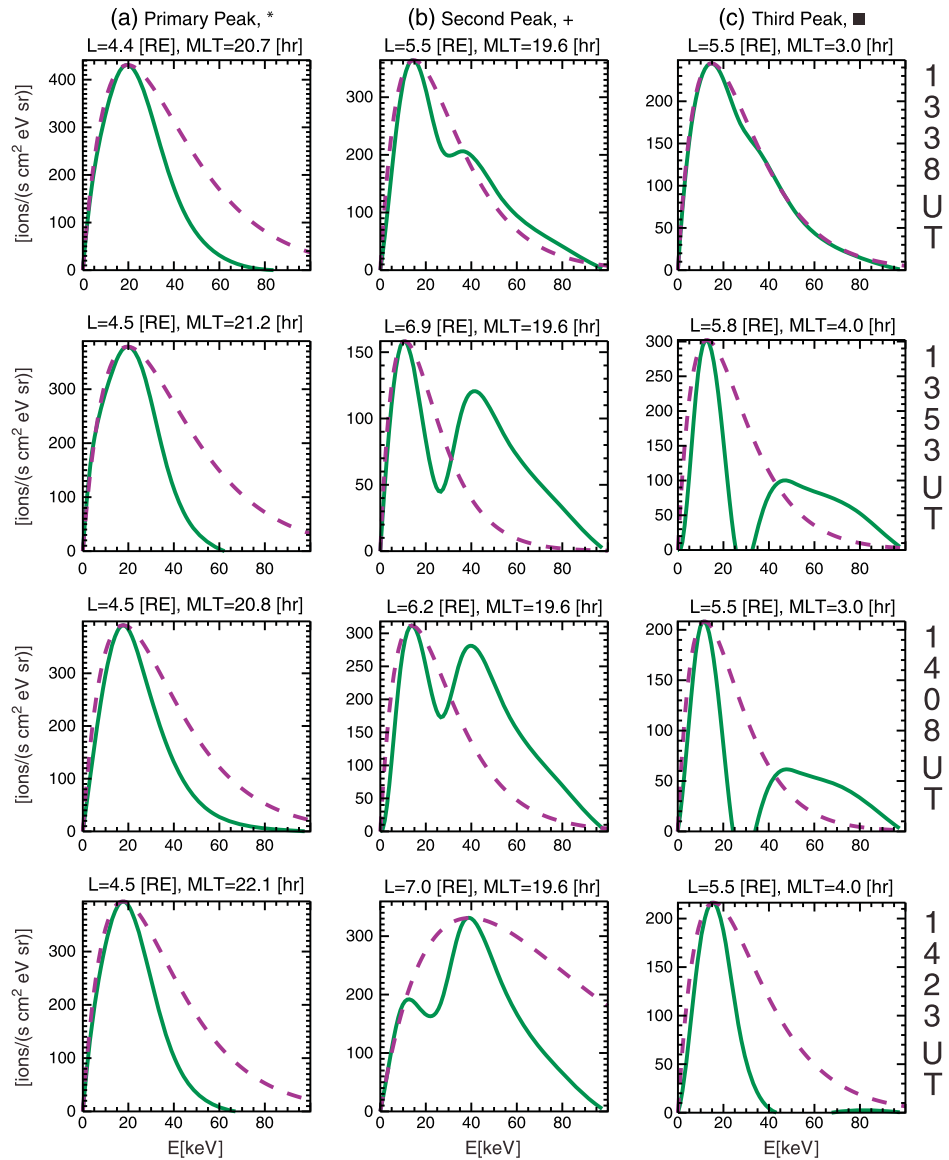
Figure 10. Energy spectra obtained from the ion flux deconvolved from TWINS 1 and 2 ENA images for 1338, 1353, 1408, 1423 UT on 29 May 2010. The green line is the TWINS energy spectrum. The purple dashed line is a Maxwellian with the same peak energy. (a) For the main peak indicated by black stars in Figure 7, the (b) center column is for the second peak indicated by black plus signs in Figure 7. (c) For the third peak indicated by black squares in Figure 7.

The stereoscopic viewing geometry for this event is shown in Figure 3b. This time TWINS 1 is at $\{-1.91, -3.32, 4.80\}$ R_E and TWINS 2 is at $\{-3.02, -2.53, 3.96\}$ R_E, i.e., both are in the midnight/dawn sector. The brightest pixels are again due to LAEs.

Figure 12 shows the equatorial pitch angle averaged ion flux at 15.0 keV deconvolved from stereoscopic TWINS 1 and TWINS 2 data for two 15 min time periods centered at 1653 and 1708 UT on 26 May 2011. There are two very clear peaks, one at about 5 R_E in the dusk/midnight sector and a second at about 6.5 R_E just past midnight. The flux is much lower than in the previous event as might be expected due to the fact that SYM/H is only -6 nT.

Figure 13 shows the ion flux energy spectra at the two peaks during the two 15 min intervals. Each has a low-energy maximum at about 10 keV and a higher-energy maximum between 40 and 60 keV. While the strength of the lower energy maximum is the same at both locations for the full half hour, the strength of the higher-energy maximum decreases with time.
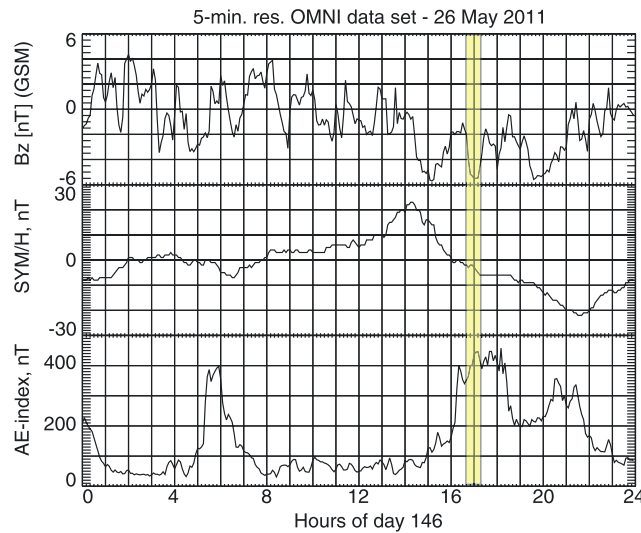
Figure 11. The z component of the interplanetary magnetic field in the GSM coordinate system scaled in time to the nose of the magnetopause and geomagnetic activity indices, *SYM/H* and *AE*, from the OMNI data website (http://omniweb.gsfc.nasa.gov/form/omni_min.html) for 26 May 2011. The time period with stereoscopic TWINS ENA images treated in this study is marked by the yellow rectangle.

4. Discussion

4.1. Event 1: 29 May 2010, 1330–1430 UT

As shown in Figure 6, this weak CIR storm's main phase started at the beginning of the day and reached its minimum between 12 and 13 h later. The time period of interest here occurred just after the recovery began. The IMF was negative during this entire time period maintaining a steady minimum of about -14 nT for 6–7 h. The *AE* index shows peaks of 1000–1500 nT during the same time period. Of particular interest here is the largest peak from 1200 to 1300 UT and peaks at about 1300 nT from 1300 to 1400 UT. These immediately precede and overlap the specific hour, i.e., 1330–1430 UT during which we have excellent TWINS 1 and TWINS 2 ENA images. The deconvolved ion flux

shown in Figure 7 has a main peak at about 4.5 R_E in the dusk/midnight sector that remains fairly steady during this time interval. A second peak in the same sector but at larger radius develops during this hour. A third peak occurs in the midnight/dawn sector between 5 and 6 R_E. The results of the study by *Gabrielse et al.* [2014] seem consistent with interpreting these multiple spatial peaks with dipolarizations and associated injections in the magnetotail and with the fact that they are more prevalent in the dusk/midnight sector. The results of the 3-D global hybrid simulation [*Lin et al.*, 2014] shown in Figure 1 predict a greater number of reconnection events that lead to injections into the inner magnetosphere in the premidnight region, but events in the postmidnight sector are also predicted. At this time the simulations are not able to resolve the structure or to follow the decay of the injected particles in the detail necessary to make direct comparisons with the deconvolved flux of trapped ring particles shown here. That will be the subject of a future investigation.

Comparisons of the ion flux obtained by deconvolving TWINS images with THEMIS in situ measurements in Figures 8 and 9 show good agreement both spatially and temporally. But the single path followed by the THEMIS satellite is, of course, not able to observe the full spatial structure obtained from the stereoscopic TWINS 1 and TWINS 2 ENA images. This clearly illustrates how global images are able to show the global structure while the in situ measurements provide local details.

Figure 14 shows the component of the magnetic field that points perpendicular to the orbit plane (aligned with Earth's spin axis for a zero-degree inclination satellite) at geosynchronous orbit as observed by GOES 11, 12, 13, and 14 from 1200 to 1800 UT on 29 May 2010. The yellow shaded box shows the measurements during the period in which we have found a spatial peak in the trapped ion population just
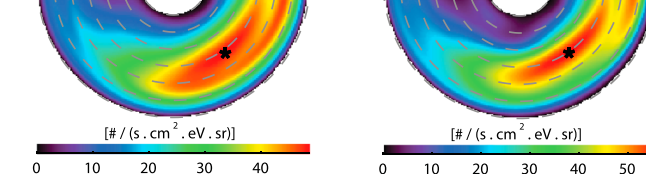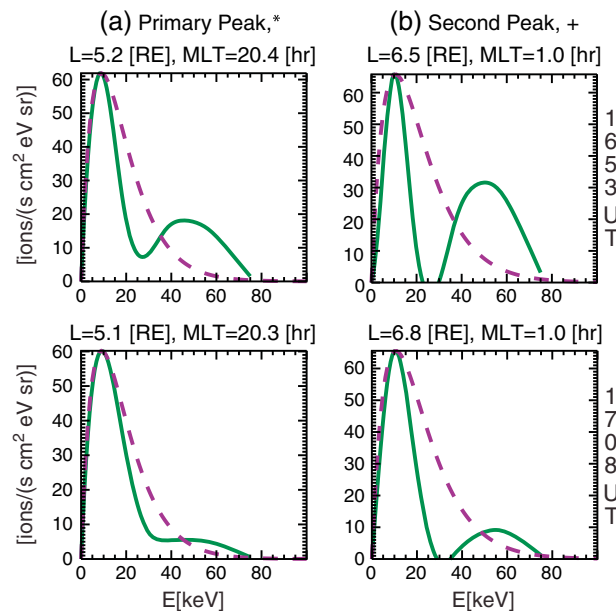

Figure 12. Equatorial pitch angle averaged ion flux at 15.0 keV on 26 May 2011 for times 1653 and 1708 UT from TWINS 1 and 2. The location of the peak of the ion flux is indicated by black stars. A second peak is indicated by black plus signs. Color bars are slightly different to emphasize the spatial distributions.

Figure 13. Energy spectra obtained from the ion flux deconvolved from TWINS 1 and 2 ENA images for 1653 and 1708 UT on 26 May 2011. The green line is the TWINS energy spectrum. The purple dashed line is a Maxwellian with the same maximum energy. (a) For the main peak indicated by black stars and (b) for the second peak indicated by black plus signs in Figure 12.

inside geosynchronous orbit in the midnight/dawn sector (see the "black square" in Figure 7). The data show strong stretching and dipolarization of the field, at all but perhaps GOES 11 (the most western satellite that is closest to midnight) in the 1200–1400 UT time interval that is consistent with the observed strong *AE* signatures (see Figure 6) and likely consistent with plasma injections at geosynchronous. In the dipolarization region, especially from GOES 14, past GOES 13, to GOES 12, the spatial peak observed by TWINS in the trapped ion population is observed immediately following the magnetic field dipolarization. The fact that these reconfigurations of the Earth's magnetic field are observed in the dawn/noon sector may have to do with the strength of this CIR-driven storm and the mapping of field lines that are likely swept tailward during this interval. Also, note that GOES 14, 13, and 12 data show that the dipolarization begins near dawn and systematically progresses toward noon. It seems likely that the stretching and snapping back of the magnetic field is related to the spatial peak (see the black square in Figure 7) in the ion flux observed in the stereoscopic TWINS images.

The energy spectra of the ions at the three peaks shown in the three columns of Figure 10 as a function of time (down the page in Figure 10) present a number of interesting features. It is to be noted that the 15 keV ion intensities shown in previous figures are integrated over the ion spectra from 7.5 to 22.5 keV. This means that the values at 15 keV in the two figures may not exactly match. For the main peak (see black star in Figure 7), the energy spectra have a maximum near 20 keV with perhaps a cooling to 17 keV during the hour. The energy dependence below the maximum is very close to a Maxwellian, but above the maximum, the observed ion flux is significantly below a Maxwellian. This could be from depletion at higher energies owing to the faster drift of higher-energy particles due to the gradient and curvature of the magnetic field. The magnitude at the maximum remains fairly steady. For the second peak (see plus signs in Figure 7), the energy spectra show significant temporal development. At the 1338 UT, the main maximum is at about 15 keV, and there is the beginning of a second maximum at about 40 keV. The energies of the two maxima remain about the same. The magnitude of the flux at the second maximum is higher when the peak in the flux moves to lower *L* values (5.5 and 6.2 at 1338 and 1408 UT, respectively) and low at higher *L* values (7.0 at both 1353 and 1423 UT). The magnitude of the higher-energy maximum relative to the lower energy maximum grows until it is relatively larger than the lower energy maximum. This has the appearance of two populations with different temperatures. The peak in the midnight/dawn sector (see black square in Figure 7) starts as a Maxwellian with a maximum at about 15 keV. A second population appears with a maximum energy near 50 keV that disappears by the end of the hour. Future plans are to combine the 3-D global hybrid simulations [*Lin et al.*, 2014] with the CIMI model [*Fok et al.*, 2014] to investigate the dynamics of the energy spectra observed here.

4.2. Event 2: 26 May 2011, 1645–1715 UT

This event is a relatively quiet period as shown in Figure 11. But during this interval there are excellent stereoscopic TWINS 1 and TWINS 2 ENA images, and the *AE* index is the highest of the day. As shown in Figure 12, the deconvolved ion flux is much weaker than in the storm period discussed in the previous subsection. Nevertheless, there is interesting spatial structure. There are two peaks of about equal strength,
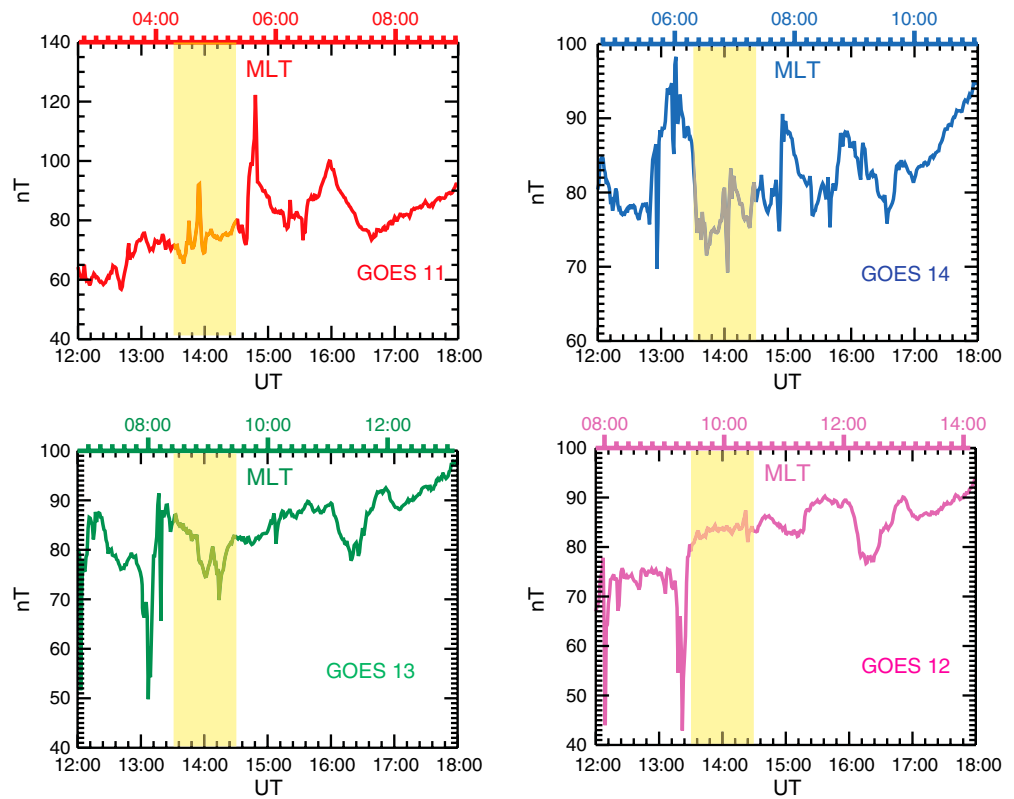
Figure 14. The z component of the magnetic field in the SM coordinate system at geosynchronous orbit on 29 May 2010 from 1200 to 2400 UT measured by GOES 11, 12, 13, and 14. The measurements from the four satellites are presented in order of longitude. The lower horizontal axis is UT and is the same for all four satellites. The upper horizontal axis shows the position of each satellite in MLT as a function of time. The transparent yellow rectangle shows the time period in which the results from stereoscopic TWINS image are presented.

one at about 5 R_E in the dusk/midnight sector and a second at about 6.5 R_E just past midnight. There is little spatial change in this relatively short time period, but the energy spectra shown in Figure 13 do vary with time. For both peaks in both time intervals, the energy maximum is near 10 keV and the energy dependence below the peak is Maxwellian. For both peaks, however, there is a high-energy maximum at about 40–50 keV that decays from the first 15 min period to the second. Again, a possible explanation is that this is due to depletion from energy-dependent drift due to magnetic field gradients and curvatures.

Neither THEMIS nor GOES was in position to provide data to compare with the results for this time period. While the statistical study of THEMIS measurements [*Gabrielse et al.*, 2014] demonstrated that multiple dipolarizations and associated injections are more likely during active geomagnetic events, it was found that such events are correlated with enhanced *AL*. This event is not a storm, but it does have enhanced *AE* activity.

5. Summary

Ion trapped ring current particle spatial, temporal, and energy-dependent results obtained from stereoscopic TWINS ENA images have been presented. For the time period 1330–1430 UT on 29 May 2010, comparison with THEMIS in situ measurements shows excellent spatial and temporal correlations illustrating the improvement in resolution when stereoscopic images are available. The global images show multiple spatial peaks whose existence is supported qualitatively by 3-D global hybrid simulations and by GOES geosynchronous measurements of the z component of the magnetic field. Energy spectra at the multiple spatial peaks of the ion flux are also presented. A lower energy maximum is seen at about 20 keV which is Maxwellian below this maximum but is below a Maxwellian above this maximum likely due to depletion at higher energies owing to energy-dependent drift. At times, a second maximum near 40 keV also is seen indicating the possibility of two plasma populations. This occurs at the beginning of the recovery phase of a CIR storm.

A second time period when the magnetosphere is relatively quiet, 1645–1715 UT on 26 May 2011, also shows multiple spatial peaks in the trapped particle ring current. The flux is much lower than in the storm event. The energy spectra at the peaks have a lower energy maximum at approximately 10 keV, also lower than the storm event, and a bump on tail at about 50 keV.

Comparison of results from single TWINS 1 and TWINS 2 ENA images with stereoscopic combinations of the two was shown to produce enhanced spatial and temporal resolution. The technique used to deconvolve ion distributions from the ENA images which is designed to produce spatial structure only when necessary to fit the data has shown multiple spatial peaks in the ions in the inner ring current. This illustrates the contribution of global imaging to understanding the connection between the inner magnetosphere and magnetotail. The observed energy spectra show evidence for energy-dependent drift and multiple plasma components.

References

Angelopoulos, V. (2008), The THEMIS mission, *Space Sci. Rev.*, *141*(1–4), 5–34, doi:10.1007/s11214-008-9336-1.

Angelopoulos, V., W. Baumjohann, C. F. Kennel, F. V. Coroniti, M. G. Kivelson, R. Pellat, R. J. Walker, H. Lühr, and G. Paschmann (1992), Bursty bulk flows in the inner central plasma sheet, *J. Geophys. Res.*, *97*(A4), 4027–4039, doi:10.1029/91JA02701.

Baumjohann, W., G. Paschmann, and H. Lühr (1990), Characteristics of high speed ion flows in the plasma sheet, *J. Geophys. Res.*, *95*(A4), 3801–3809, doi:10.1029/JA095iA04p03801.

Bazell, D., E. C. Roelof, T. Sotirelis, P. C. Brandt, H. Nair, P. Valek, J. Goldstein, and D. McComas (2010), Comparison of TWINS images of low-altitude emission of energetic neutral atoms with DMSP precipitating ion fluxes, *J. Geophys. Res.*, *115*, A10204, doi:10.1029/2010JA015644.

Belian, R. D., T. E. Cayton, and G. D. Reeves (1995), Quasi-periodic, substorm associated, global flux variations observed at geosynchronous orbit, in *Space Plasmas: Coupling Between Small and Medium Scale Processes*, *Geophys. Monogr. Ser.*, vol. 86, edited by M. Ashour-Abdalla, T. Chang, and P. Dusenbery, 143 pp., AGU, Washington, D. C.

Birn, J., R. Nakamura, E. V. Panov, and M. Hesse (2011), Bursty bulk flows and dipolarization in MHD simulations of magnetotail reconnection, *J. Geophys. Res.*, *116*, A01210, doi:10.1029/2010JA016083.

Burch, J. L. (2000), IMAGE Mission Overview, *Space Sci. Rev.*, *91*, 1.

Chen, C. X., and R. A. Wolf (1993), Interpretation of high-speed flows in the plasma sheet, *J. Geophys. Res.*, *98*(A12), 21,409–21,419, doi:10.1029/93JA02080.

Chen, C. X., and R. A. Wolf (1999), Theory of thin-filament motion in Earth's magnetotail and its application to bursty bulk flows, *J. Geophys. Res.*, *104*(A7), 14,613–14,626, doi:10.1029/1999JA900005.

C:son Brandt, P., R. Demajistre, E. C. Roelof, S. Ohtani, D. G. Mitchell, and S. Mende (2002a), IMAGE/high-energy energetic neutral atom: Global energetic neutral atom imaging of the plasma sheet and ring current during substorms, *J. Geophys. Res.*, *107*(A12), 1454, doi:10.1029/2002JA009307.

C:son Brandt, P., S. Ohtani, D. G. Mitchell, M.-C. Fok, E. C. Roelof, and R. Demajistre (2002b), Global ENA observations of the storm main phase ring current: Implications for skewed electric fields in the inner magnetosphere, *Geophys. Res. Lett.*, *29*(20), 1954, doi:10.1029/2002GL015160.

C:son Brandt, P., S. Ohtani, D. G. Mitchell, R. Demajistre, and E. C. Roelof (2002c), ENA observations of a global substorm growth phase dropout in the nightside magnetosphere, *Geophys. Res. Lett.*, *29*(20), 1962, doi:10.1029/2002GL015057.

C:son Brandt, P., E. C. Roelof, S. Ohtani, D. G. Mitchell, and B. Anderson (2004), IMAGE/HENA: Pressure and current distributions during the 1 October 2002 storm, *Adv. Space Res.*, *33*, 719.

deBoor, C. (1978), *A Practical Guide to Splines*, Springer, New York, doi:10.1007/978-1-4612-6333-3.

DeMajistre, R., E. C. Roelof, P. C:son Brandt, and D. G. Mitchell (2004), Retrieval of global magnetospheric ion distributions from high-energy neutral atom measurements made by the IMAGE/HENA instrument, *J. Geophys. Res.*, *109*, A04214, doi:10.1029/2003JA010322.

Erickson, G. M., and R. A. Wolf (1980), Is steady convection possible in the Earth's magnetotail?, *Geophys. Res. Lett.*, *7*, 897–900, doi:10.1029/GL007i011p00897.

Farris, M. H., and C. T. Russell (1994), Determining the standoff distance of the bow shock: Mach number dependence and use of models, *J. Geophys. Res.*, *99*(A9), 17,681–17,689, doi:10.1029/94JA01020.

Fok, M.-C., N. Y. Buzulukova, S.-H. Chen, A. Glocer, T. Nagai, P. Valek, and J. D. Perez (2014), The Comprehensive Inner-Magnetosphere Ionosphere (CIMI) model, *J. Geophys. Res. Space Physics*, *119*, 7522–7540, doi:10.1002/2014JA020239.

Gabrielse, C., V. Angelopoulos, A. Runov, and D. L. Turner (2014), Statistical characteristics of particle injections throughout the equatorial magnetotail, *J. Geophys. Res. Space Physics*, *119*, 2512–2535, doi:10.1002/2013JA019638.

Goldstein, J., and D. J. McComas (2013), Five years of stereo magnetospheric imaging by TWINS, *Space Sci. Rev.*, *180*, 39, doi:10.1007/s11214-013-0012-8.

Goodrich, C. C., T. I. Pulkkinen, J. G. Lyon, and V. G. Merkin (2007), Magnetospheric convection during intermediate driving: Sawtooth events and steady convection intervals as seen in Lyon-Fedder-Mobarry global MHD simulations, *J. Geophys. Res.*, *112*, A08201, doi:10.1029/2006JA012155.

Grimes, E. W., J. D. Perez, J. Goldstein, D. J. McComas, P. Valek, and D. Turner (2013), Comparison of TWINS and THEMIS observations of proton pitch angle distributions in the ring current during the 29 May 2010 geomagnetic storm, *J. Geophys. Res. Space Physics*, *118*, 4895–4905, doi:10.1002/jgra.50455.

Henderson, M. G., G. D. Reeves, R. M. Skoug, M. F. Thomsen, M. H. Denton, S. B. Mende, T. J. Immel, P. C. Brandt, and H. J. Singer (2006a), Magnetospheric and auroral activity during the 18 April 2002 sawtooth event, *J. Geophys. Res.*, *111*, A01S90, doi:10.1029/2005JA011111.

Henderson, M. G., et al. (2006b), Substorms during the 10–11 August 2000 sawtooth event, *J. Geophys. Res.*, *111*, A06206, doi:10.1029/2005JA011366.

Huang, C.-S., J. C. Foster, G. D. Reeves, G. Le, H. U. Frey, C. J. Pollock, and J.-M. Jahn (2003), Periodic magnetospheric substorms: Multiple space-based and ground-based instrumental observations, *J. Geophys. Res.*, *108*(A11), 1411, doi:10.1029/2002JA009992.

Keesee, A. M., M. W. Chen, E. E. Scime, and A. T. Y. Lui (2014), Regions of ion energization observed during the Galaxy-15 substorm with TWINS, *J. Geophys. Res. Space Physics*, *119*, 8274–8287, doi:10.1002/2014JA020466.

Lin, Y., X. Y. Wang, S. Lu, J. D. Perez, and Q. Lu (2014), Investigation of storm time magnetotail and ion injection using three-dimensional global hybrid simulation, *J. Geophys. Res. Space Physics*, *119*, 7413–7432, doi:10.1002/2014JA020005.

McComas, D. J., H. O. Funsten, and E. E. Scime (1998), Advances in low energy neutral atom imaging, in *Measurement Techniques in Space Plasmas-Fields*, Geophys. Monogr. Ser., vol. 103, edited by R. F. Pfaff, J. E. Borovsky, and D. T. Young, pp. 275–280, AGU, Washington, D. C.

McComas, D. J., et al. (2009a), The two wide-angle imaging neutral-atom spectrometers (TWINS) NASA mission-of-opportunity, *Space Sci. Rev.*, *142*, 157–231, doi:10.1007/s11214-008-9467-4.

McComas, D. J., et al. (2009b), Global observations of the interstellar interaction from the Interstellar Boundary Explorer (IBEX), *Science*, *326*, 959–962, doi:10.1126/science.1180906.

McComas, D. J., N. Buzulukova, M. G. Connors, M. A. Dayeh, J. Goldstein, H. O. Funsten, S. Fuselier, N. A. Schwadron, and P. Valek (2012), TWINS and IBEX ENA imaging of the 5 April 2010 substorm, *J. Geophys. Res.*, *117*, A03225, doi:10.1029/2011JA017273.

McFadden, J. P., C. W. Carlson, D. Larson, M. Ludlam, R. Abiad, B. Elliot, P. Turin, M. Marckwordt, and V. Angelopoulos (2008), The THEMIS ESA plasma instrument and in-flight calibration, *Space Sci. Rev.*, *141*, 277–302, doi:10.1007/s11214-008-9440-2.

Mitchell, D. G., et al. (2000), High Energy Neutral Atom (HENA) imager for the IMAGE mission, *Space Sci. Rev.*, *91*, 67.

Perez, J. D., G. Kozlowski, P. C:son-Brandt, D. G. Mitchell, J.-M. Jahn, C. J. Pollock, and X.-X. Zhang (2001), Initial ion equatorial pitch angle distributions from medium and high energy neutral atom images obtained by IMAGE, *Geophys. Res. Lett.*, *22*, 1155–1158, doi:10.1029/2000GL012636.

Perez, J. D., X.-X. Zhang, P. C:son Brandt, D. G. Mitchell, J.-M. Jahn, and C. J. Pollock (2004a), Dynamics of ring current ions as obtained from IMAGE HENA and MENA ENA images, *J. Geophys. Res.*, *109*, A05208, doi:10.1029/2003JA010164.

Perez, J. D., X.-X. Zhang, P. C:son Brandt, D. G. Mitchell, J.-M. Jahn, C. J. Pollock, and S. B. Mende (2004b), Trapped and precipitating protons in the inner magnetosphere as seen by IMAGE, *J. Geophys. Res.*, *109*, A09202, doi:10.1029/2004JA010421.

Perez, J. D., E. W. Grimes, J. Goldstein, D. J. McComas, P. Valek, and N. Billor (2012), Evolution of CIR storm on 22 July 2009, *J. Geophys. Res.*, *117*, A09221, doi:10.1029/2012JA017572.

Pollock, C. J., et al. (2000), Medium energy neutral atom (MENA) imager for the IMAGE mission, *Space Sci. Rev.*, *91*, 113–154.

Pontius, D. H., Jr., and R. A. Wolf (1990), Transient flux tubes in the terrestrial magnetosphere, *Geophys. Res. Lett.*, *17*, 49–52, doi:10.1029/GL017i001p00049.

Roelof, E. C. (1997), ENA emission from nearly mirroring magnetospheric ions interacting with the exosphere, *Adv. Space Res.*, *20*, 361–366.

Russell, C. T. (1971), Geophysical Coordinate Transformations, *Cosmic Electrodynamics*, *2*, 184.

Sergeev, V. A., V. Angelopoulos, J. T. Gosling, C. A. Cattell, and C. T. Russell (1996), Detection of localized, plasma-depleted flux tubes or bubbles in the midtail plasma sheet, *J. Geophys. Res.*, *101*(A5), 10,817–10,826, doi:10.1029/96JA00460.

Shue, J.-H., J. K. Chao, H. C. Fu, C. T. Russell, P. Song, K. K. Khurana, and H. J. Singer (1997), A new functional form to study the solar wind control of the magnetopause size and shape, *J. Geophys. Res.*, *102*(A5), 9497–9511, doi:10.1029/97JA00196.

Thomsen, M. F., J. Birn, J. E. Borovsky, K. Morzinski, D. J. McComas, and G. D. Reeves (2001), Two-satellite observations of substorm injections at geosynchronous orbit, *J. Geophys. Res.*, *106*(A5), 8405–8416, doi:10.1029/2000JA000080.

Toffoletto, F. R., S. Sazykin, R. Spiro, and R. Wolf (2003), Inner magnetospheric modeling with the Rice Convection Model, *Space Sci. Rev.*, *107*, 175–196, doi:10.1023/A:1025532008047.

Tsyganenko, N. A., and M. I. Sitnov (2005), Modeling the dynamics of the inner magnetosphere during strong geomagnetic storms, *J. Geophys. Res.*, *110*, A03208, doi:10.1029/2004JA010798.

Vallat, C., et al. (2004), First comparisons of local ion measurements in the inner magnetosphere with energetic neutral atom magnetospheric image inversions: Cluster-CIS and IMAGE-HENA observations, *J. Geophys. Res.*, *109*, A04213, doi:10.1029/2003JA010224.

Wahba, G. (1990), Spline models for observational data, Soc. for Ind. and Appl. Math., Philadelphia, Pa., doi:10.1137/1.9781611970128.

Yang, J., F. R. Toffoletto, R. A. Wolf, and S. Sazykin (2011), RCM-E simulation of ion acceleration during an idealized plasma sheet bubble injection, *J. Geophys. Res.*, *116*, A05207, doi:10.1029/2010JA016346.

Zaharia, S., V. K. Jordanova, M. F. Thomsen, and G. D. Reeves (2006), Self-consistent modeling of magnetic fields and plasmas in the inner magnetosphere: Application to a geomagnetic storm, *J. Geophys. Res.*, *111*, A11S14, doi:10.1029/2006JA011619.

Zhang, X. X., J. D. Perez, T. Chen, C. Wang, P. C. Brandt, D. G. Mitchell, and Y. L. Wang (2005), Proton temperatures in the ring current from ENA images and in situ measurements, *Geophys. Res. Lett.*, *32*, L16101, doi:10.1029/2005GL023481.

Zoennchen, J. H., U. Nass, and H. J. Fahr (2013), Exospheric hydrogen density distributions for equinox and summer solstice observed with TWINS1/2 during solar minimum, *Ann. Geophys.*, *31*, 513–527, doi:10.5194/angeo-31-513-2013.